An alternative method to measure corrosion rate of reinforced concrete structures

Gabriel Samson, Fabrice Deby, Jean-Luc Garciaz, Mansour Lassoued

An alternative method to measure corrosion rate of reinforced concrete structures

Gabriel Samson[1], Fabrice Deby[1], Jean-Luc Garciaz[2], Mansour Lassoued[2]

[1] *LMDC, INSAT/UPS Génie Civil, 135 Avenue de Rangueil, 31077 Toulouse cedex 04 France.*

[2] *LERM SETEC, 23 Rue de la Madeleine, 13631 Arles cedex France*

Abstract

A new probe, which does not use a confinement ring, has been developed to assess the corrosion state of reinforced concrete structures. Galvanostatic polarization is performed and the rebar corrosion potential, concrete resistivity and rebar corrosion rate are evaluated using an iterative calculation algorithm. The surface linear polarization resistance ($R_{P,s} = \Delta E_P/j_{PI}$) of the rebar / concrete interface is calculated by converting the potential measured at the surface into the rebar polarization ΔE_P and the current density at the point of interest (PI) j_{PI} using 3D numerical simulations. The calculation involves three geometrical parameters that modify the current and potential distribution in the concrete: the rebar spacing, s; the concrete cover, c; and the rebar diameter, D. Concrete cover resistivity is calculated using the instantaneous ohmic drop measured at the beginning of the galvanostatic polarization and the rebar corrosion rate is calculated using the steady-state potential. As the rebar corrosion rate also modifies the potential distribution in concrete, an iterative methodology was developed, using different supposed corrosion rates. Finally, the probe and associated methodology were used to evaluate the corrosion state of eight concrete slabs. Half of them were prepared with chloride in order to initiate corrosion. Four slabs were stored outdoors, two indoors in an ordinary laboratory environment and two indoors in a 50% CO_2 gas chamber. The three corrosion parameters evaluated (corrosion potential, concrete cover resistivity and rebar corrosion rate) were in good agreement with the composition of the slabs and their curing conditions.

Highlights

- A new probe to assess corrosion rate of reinforced concrete structure was developed

- The linear polarization resistance $R_{P,s}$ is calculated using 3D numerical simulations

- Rebar spacing, concrete cover and resistivity modify the potential distribution

Keywords

Corrosion rate, reinforced concrete structure, surface linear polarization resistance (SLPR), 3D numerical simulation, point of interest (PI), iterative methodology.

Corresponding authors

Gabriel Samson: samson@insa-toulouse.fr

Fabrice Deby: fabrice.deby@insa-toulouse.fr

Funding

DIAMOND is a collaborative R&D project supported by the French government's FUI program, Direction Générale des Entreprises, BPI France and PACA regional council, and accredited by four competitiveness clusters: SAFE, Mer Méditerranée, Nuclear Valley and Alpha RLH.

1 Introduction

Steel corrosion is the main cause of deterioration in reinforced concrete structures and the high cost of repairs is responsible for considerable financial losses [1,2]. Corrosion detection and the evaluation of its kinetics could optimize the maintenance of such structures and increase users' safety.

A passive layer formed in the high pH of the surrounding concrete initially protects steel rebars from corroding. However, under certain conditions, this protective layer can be locally (macro-cell corrosion) or totally (uniform corrosion) destroyed. Macro-cell corrosion is usually caused by local chloride ingress from the external environment (de-icing salts or marine environment) while uniform corrosion results from the penetration of CO_2 from the atmosphere (concrete carbonation) [3], although coupling with passive armatures can lead to macro-cell currents. The theory developed in this article assumes uniform corrosion.

Different physical parameters are relevant to assess the corrosion state of a reinforced concrete structure: half-cell corrosion potential, E_{corr}; concrete resistivity, ρ; or rebar corrosion rate, i_{corr}. Corrosion potential measurement evaluates the risk of corrosion [4]. Concrete cover resistivity is increasingly being considered as a durability index for assessing the long-term performance of concrete structures [2-4]. Such resistivity can be measured by the device presented in this article and details of the measurement principle are to be found in [8]. It is usually considered that concrete resistivity and corrosion rate are inversely proportional [9,10]. However, in an extensive review article, Horbostel et al. [11] demonstrated that the relation established cannot be unique as it depends on several parameters. This explains the growing interest of assessing corrosion by more quantified techniques than the corrosion potential or resistivity measurements and has led to several publications dealing with corrosion rate [1,2,12–16]. The corrosion rate of steel plays an important role in safety evaluations, maintenance decisions and residual life predictions for the existing RC structures

[13]. The rebar corrosion rate, i_{corr}, depends on the binder composition, moisture content, concrete resistivity, pore solution pH, temperature, and dissolved oxygen concentration [14,17–21], all of which can evolve with time, depending on the concrete exposure conditions.

Most of the time, corrosion rate, which can also be called corrosion current density, is estimated by determining the linear polarization resistance R_P (LPR). Polarization is a transient phenomenon. In the steady state, the relation between the rebar polarization, ΔE_P ($\Delta E_P = E - E_{corr}$ [V]), and the current density, i [A.m^{-2}], flowing through the interface is governed by the non-linear Butler-Volmer equation:

$$i = i_{corr}\left(e^{\ln(10)\frac{E-E_{corr}}{b_a}} - e^{\ln(10)\frac{E-E_{corr}}{b_c}}\right) \qquad \text{Eq. 1}$$

where i_{corr} [A.m^{-2}] is the corrosion rate, and b_a and b_c [V] are the Tafel slopes [22]. The LPR is the ratio of a small rebar polarization, ΔE_P, to the current flowing through the concrete / steel interface in the steady state. It is generally considered that a maximum rebar polarization ΔE_P of 20 mV enables the curve to stay on the linear part of the Butler-Volmer equation and guarantees the reversibility of the measurement. Stern and Geary [23] proposed an empirical relation between corrosion rate and the LPR R_P [Ω] :

$$i_{corr} = \frac{B}{R_P A} \qquad \text{Eq. 2}$$

where surface area A is taken to be the uniformly polarized area of the steel. This equation can only be used for uniform corrosion. B is a proportionality constant. It depends on the anodic and cathodic Tafel slopes, b_a and b_c respectively:

$$B = \frac{b_a b_c}{\ln(10)(b_a + b_c)} \qquad \text{Eq. 3}$$

Usually, B is assumed to be 26 mV for passive rebars and 52 mV for active ones [16]. However, as far as we know, these parameters cannot be measured on site with non-

destructive tests and large variations of these parameters have been demonstrated with Tafel analysis on cylinders [24–26].

Various methods exist to determine the LPR on site: galvanostatic [27], potentiodynamic [27,28], coulostatic [29] or CEPRA methods [15]. Most of the time, on site, the LPR is measured according to the RILEM TC 154-EMC [16] recommendations in which a confinement ring is employed. However, this method is based on two strong hypotheses that do not hold true on site. First, the rebar is assumed to be uniformly polarized. Several studies, usually based on numerical simulation, have proved that this is not the case. The point of the rebar right under the polarizing probe is the most polarized [30–33]. In the present study, this point will be referred to as the point of interest (PI).

Commercial devices are usually used to determine the polarization resistance. They are based on a confinement technique (a guard ring) in order to control the polarized area and confine the current to a well-defined area A (see Eq. 2) of the steel rebar [12]. In a recent study, Fahim et al. [15] compared two devices and showed that they were not able to calculate the corrosion rate for the passive state, while satisfactory results were obtained for the active state. Other investigations have revealed that different corrosion rates are obtained when these commercial devices are used [34–37]. The main reason for the discrepancies is attributed to confinement problems [38,39]. Nygaard et al. [34] developed a quantitative method to assess confinement techniques, which indicated that, for a passive rebar, the actual corrosion rate calculated by a commercial device was approximately 10 times too high, while it was 100 times too high for another device because these instruments were not able to confine current. Thus, a new solution is needed.

This work was carried out as part of the DIAMOND project [40], which aims to create a new electrochemical device to assess the corrosion state of reinforced concrete structures by measuring half-cell corrosion potential, concrete resistivity and corrosion rate simultaneously

with the same device. The probe geometry is simpler as no guard ring is employed. The corrosion rate calculation is based on three-dimensional numerical simulations that take several geometrical parameters into account (concrete cover and resistivity, rebar diameter and spacing). In addition, an iterative method is developed to evaluate the corrosion rate as this parameter also modifies the distribution of current lines in the system.

The present study focusses on corrosion rate assessment. The concrete cover resistivity measurement method was described in detail in [8]. Here the DIAMOND probe for on-site measurements will be presented first and will be used to identify the corrosion state of rebars embedded in concrete slabs that are presented later. The measurement methodology will then be introduced, with numerical modelling of the measurement using COMSOL software and presentation of the numerical results. Finally, the experimental results will be presented and discussed.

2 Materials

2.1 DIAMOND probe characteristics

Figure 1 (a) shows a picture of the DIAMOND probe and a schematic layout is given in Figure 1 (b). The DIAMOND probe consists of a cylindrical probe in which a galvanostat is inserted (unlike the previous prototype probe presented in [8], where an external galvanostat was used for measurements). The cylinder is 50 mm in diameter and 130 mm high and weighs 182 grams. The measuring device was designed with reduced size and load in order to facilitate on site measurements. The Counter Electrode (CE) is a 22 mm diameter disk of 1 mm diameter silver wire wrapped in a spiral around a central space where the 5 mm diameter. Reference Electrode (RE) is placed in order to register the potential on the concrete surface. The electrical continuity between the RE and the concrete surface is provided by a non-shrink mortar stuck on the CE and a 1 mm thick sponge in contact with the concrete surface. To

perform the measurement, the probe is then electrically connected to the reinforcement network that constitutes the working electrode (WE).

The probe is linked to a portable tablet with a software developed by the authors on Excel. The software controls the test, provides the signal required for polarization and registers the potential on the RE. After the end of the test, the potential values measured on the RE are automatically used to calculate the concrete cover resistivity and the rebar corrosion rate. The concrete cover resistivity calculation was detailed in [8] and the corrosion rate evaluation method is detailed in this article (part 5).

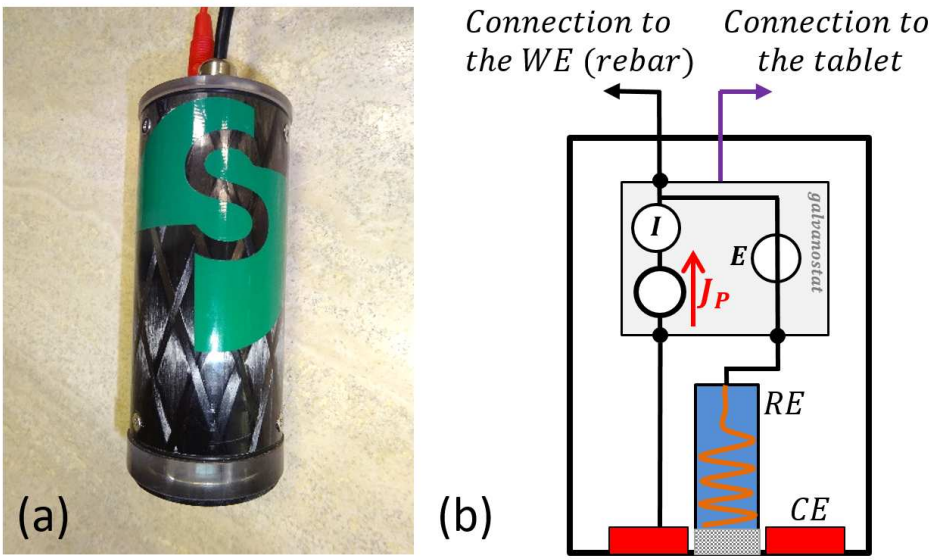

Figure 1. DIAMOND probe: side view (a), schematic layout (b).

A typical polarization curve recorded during on-site measurement is presented in Figure 2. Before the polarization, a galvanostatic pulse current of 10 µA is applied. Depending on the response, the galvanostatic current (from 1 to 25 µA) is automatically calculated for the transient polarization. The galvanostatic polarization is then applied. If the potential measured is not stabilized (less than 0.1 mV of variation during 20 seconds) after 60 seconds (which is always the case for passive rebar) curve fitting is performed using is a typical exponential charging RC circuit (Randles model) and the potential is estimated at 300 seconds [41]. The data recorded are then converted into the output data of interest to quantify the corrosion state

of the reinforced concrete structure under inspection: corrosion potential, concrete cover resistivity and corrosion rate of the rebar. The instantaneous ohmic drop is converted into concrete cover resistivity as presented in [8] and the steady-state response is used to determine the rebar corrosion rate. This conversion process is based on graphs obtained with numerical simulation and will be presented later (in part 5). The conversion requires the rebar diameter, concrete cover and rebar spacing to be manually entered in the software as they are used in the numerical simulation.

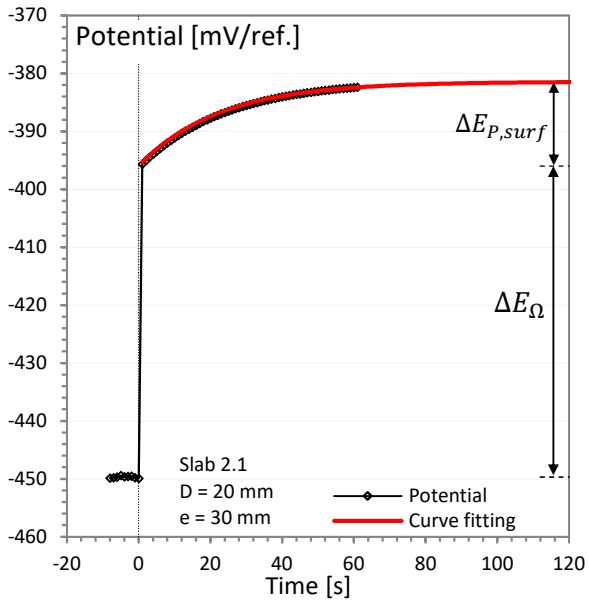

Figure 2. Typical polarization curve measured on-site by the probe.

2.2 Concrete slabs for experimental measurements

The probe and the developed method were used to evaluate the corrosion state of rebars embedded in various slabs. The slabs, 100 x 240 x 480 mm^3, were prepared using CEM I cement and a very high water/cement ratio of 1.05 in order to promote fast moisture balancing in the material. Half of the slabs were prepared with 5% NaCl (of the cement mass) in order to avoid the initiation phase of corrosion and to start immediately the propagation phase. Each slab contained three similar rebars placed at concrete cover depths of 10, 20 and 30 mm. Slabs can also be returned which enable to investigate three other concrete covers (i.e. 64, 74 and 84

mm as seen in Figure 3 for a rebar diameter of 10 mm).Two rebar diameters, 6 and 20 mm, were employed. Six polymer heat shrink tubes were placed on each slab where the rebars came out, so as to prevent water ingress and corrosion along the rebar from outside. A picture of a slab is presented in Figure 4.

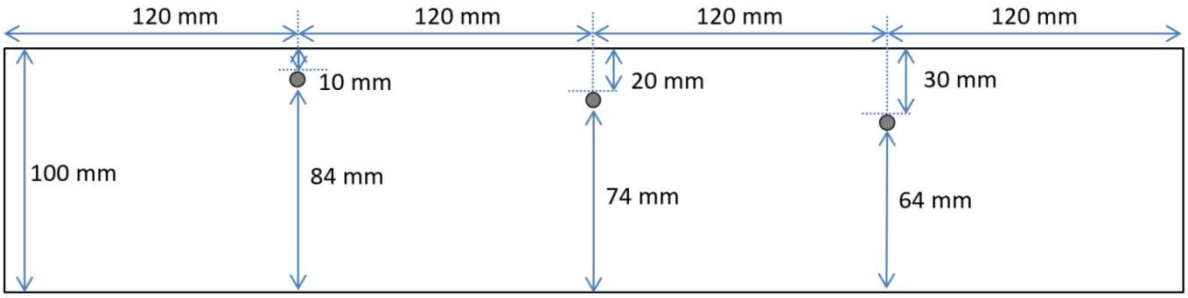

Figure 3. Side view of the slabs prepared with 6 mm diameter rebar.

Figure 4. Picture of a slab (D = 6 mm - slab placed outdoors).

All the samples were cured for 28 days under wet conditions (20°C, 95% RH). Then, four different curing conditions were applied for six months before the measurements started:

- Cure 1: Slabs outdoors, no chloride
- Cure 2: Slabs outdoors, with chloride
- Cure 3: Indoors, no chloride, placed in a 50% CO_2 carbonation chamber with around 65% RH
- Cure 4: Indoors, with chloride. Temperature 20°C, relative humidity not controlled

For each type of curing conditions, one slab was prepared with three 6 mm diameter rebars and a second slab was prepared with three 20 mm diameter rebars. The slabs placed outdoors were stored at LMDC Toulouse (France). The aim of this article is not to investigate the influence of these different curing conditions on the concrete properties but to create various extreme cases leading to different corrosion states.

3 Methodology

The schematic layout of the probe and the three steps of the polarization process are detailed in Figure 5. An electrical connection to the rebar must be made. The rebar diameter D [m] and cover thickness c [m] can be measured when the electrical connection is set up or evaluated by non-destructive techniques [42].

An equivalent electrical circuit is presented in Figure 5 (a). The concrete can be electrically modelled by a resistance R_{Ω}. The rebar / concrete interface is modelled by a Randles model associating a capacitance C and the LPR R_P in parallel. Note that this electrical circuit is a simplified representation of the 3D problem. In order to visualize the three steps of the measurement, several absolute potentials, φ, are introduced in the four parts of Figure 5. These absolute potentials cannot be measured; only measurement of the difference between two absolute potentials is possible. The reference potential E_{ref} of the RE is the difference between the absolute potential $\varphi_{m,ref}$ of the metal used in the probe (Cu) and its surrounding solution $\varphi_{sol,ref}$ ($CuSO_4$).

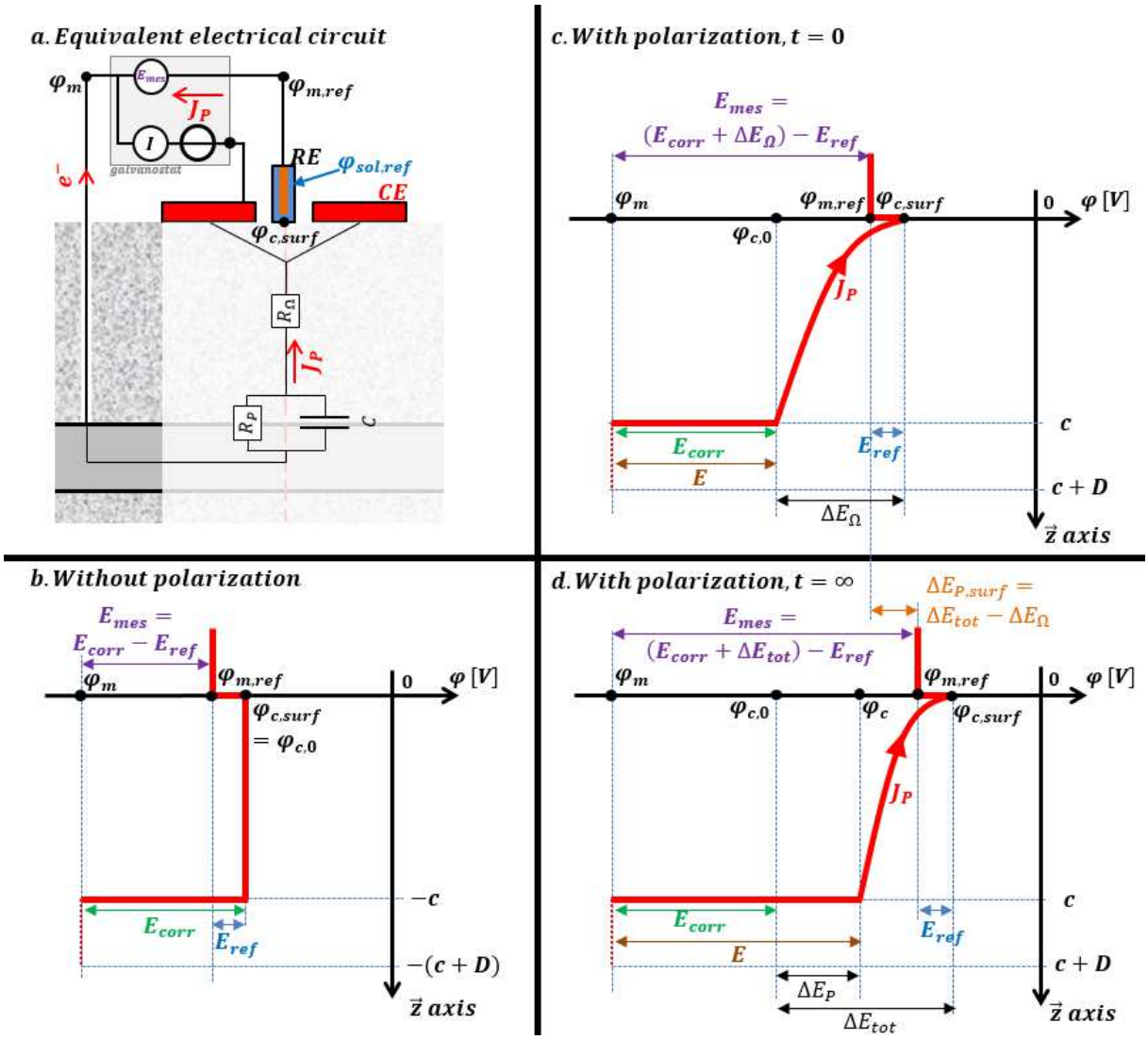

Figure 5. Equivalent electrical circuit (a). Absolute potential evolution without polarization (b), with polarization, t = 0 (c), and with polarization, t = ∞ (d).

The electrical continuity between the concrete surface and the surrounding solution of the probe is obtained with a mortar without shrinkage stuck on the CE and a 1 mm thick sponge. The absolute potential in the surrounding solution of the RE $\varphi_{sol,ref}$ is then equal to the absolute potential of the concrete in the surface $\varphi_{c,surf}$ as there is no significant resistance between these two media.

The corrosion potential E_{corr} (half-cell rebar / concrete) is the difference between the surrounding concrete absolute potential without polarization, $\varphi_{c,0}$, and the metal rebar absolute potential, φ_m.

The electrical potential evolution along the vertical, $\vec{z}$ axis is presented in the last three parts of Figure 5. The $\vec{z}$ axis is defined as the axis passing through the centre of the probe on the surface and the PI. It is represented in red in Figure 6. Without any polarization, the potential measured by the RE is the difference between the corrosion potential, E_{corr}, and the reference potential, E_{ref}, (Figure 5 (b)).

When the galvanostatic current is applied (Figure 5 (c)), the potential of the rebar / concrete interface remains equal to the corrosion potential as the capacitance of the Randles model is short-circuited. The instantaneous ohmic drop, ΔE_{Ω}, measured by the RE is due only to the concrete resistance, R_{Ω}. A previous study exploited this ohmic drop to determine the concrete cover resistivity. It was shown that the ohmic drop measured depended on the concrete resistivity and cover and also on the rebar diameter. It was also demonstrated that the rebar spacing had no significant influence.

The schematic layout of the potential of the system, in the steady state, is presented in Figure 5 (d). At steady state, the capacitance acts as an infinite resistance. The potential in the rebar / concrete interface is no longer equal to the corrosion potential. The polarization of the rebar, $\Delta E_P = E - E_{corr}$, is different from zero. The relation between the current flowing through the interface and its polarization is governed by the Butler-Volmer equation (Eq. 1). In the steady state, the rebar polarization reaches its maximum value, ΔE_P. The difference between the potential measured on the surface, ΔE_{tot}, and the instantaneous ohmic drop, ΔE_{Ω}, is the polarization measured on the surface, $\Delta E_{P,surf}$, and it is not equal to the rebar polarization ΔE_P because of the 3D nature of the problem (Figure 5 (d)).

The potential measured on the surface is influenced by both the concrete resistance R_{Ω} and the rebar / concrete interface LPR R_P. As demonstrated for the instantaneous ohmic drop, the steady-state response will also depend on the geometrical parameters of the study, the concrete cover, the rebar diameter and the concrete resistivity. Moreover, rebar spacing will

also influence the rebar polarization at the PI. The 3D numerical model developed on Comsol will be used below to convert the data measured on the surface, after the instantaneous ohmic drop and at steady-state, to determine the rebar corrosion rate, i_{corr}.

4 Finite element model

The two steps of the polarization (instantaneous ohmic drop - Figure 5 (c); steady state - Figure 5 (d)) were modelled with Comsol Multiphysics finite element model software. The AC/DC toolbox was used to evaluate current and potential distribution in the modelled geometry. The transient phase of the polarization was not modelled.

4.1 Geometry

The geometry of the model is presented in Figure 6 for an example where the concrete cover, c, is 60 mm, the rebar diameter is 10 mm and the rebar spacing is 100 mm. In all the simulations, the concrete slab is 300 mm high and 800 mm wide. As the problem exhibits double symmetry, only a quarter of the slab is modelled. The probe is placed at the centre of the slab above the central rebar. The probe model is shown in greater detail in the corner of Figure 6. The point directly under the probe, at the interface of the top face of the rebar, is the PI.

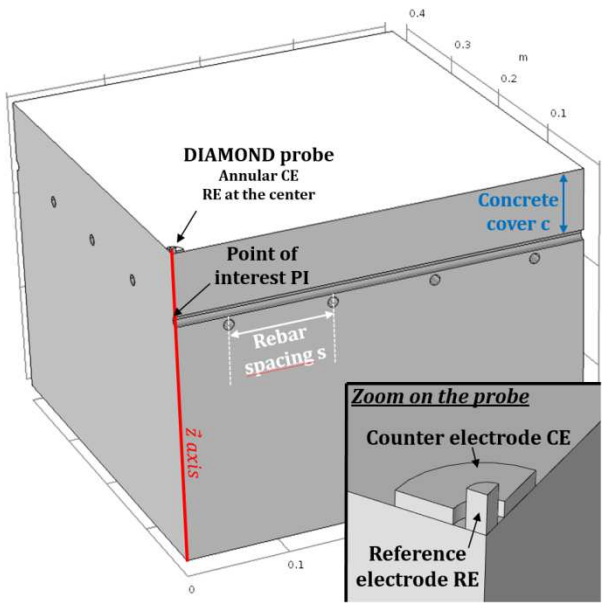

Figure 6. Modelling geometry. In this example D = 10 mm, c = 60 mm and s = 100 m. Zoom on the modelled probe in the corner.

The annular CE and the cylindrical RE are both modelled with a material having a high electrical conductivity of 10^5 S/m. The current (J_P = 10 µA) is injected on the top face of the CE. It is constant for all the numerical simulations presented in this article. The rebar framework is modelled with regularly spaced, perpendicular hollow cylinders. The cylinders are electrically connected. The central cylinder with the PI on its top face, right under the probe, is always present while other cylinders can be added to model more or less dense rebar frameworks by modifying the rebar spacing, s. Three geometrical parameters were modified in the present study: rebar spacing, s; concrete cover, c; and rebar diameter, D. The different values of the modelled geometry parameters are presented in Table 1. A wide range of these geometrical parameters was modelled in order to consider all the configurations that can be found on site. Setting the rebar diameter to infinity is equivalent to modelling a metal plate. The infinity rebar spacing corresponds to a single rebar.

Table 1. Variable parameters considered in the numerical simulations.

Parameter	Symbol	Unit	Number of values	Values
Corrosion rate	i_{corr}	µA/cm^2	3	0.1, 0.5, 1
Concrete resistivity	ρ	Ω.m	17	20, 40, 60, 80, 100, 200, 300, 400, 500, 600, 800, 1000, 1500, 2000, 4000, 6000, 10000
Rebar spacing	s	mm	5	∞, 250, 200, 150, 100
Concrete cover	c	mm	11	10, 15, 20, 25, 30, 35, 40, 50, 60, 80, 100
Rebar diameter	D	mm	10	6, 8, 10, 12, 14, 16, 20, 25, 32, ∞

4.2 Constitutive law, boundary conditions, electrochemical parameters and mesh size

In the model, concrete is assumed to be a homogeneous and isotropic material having a uniform electrical resistivity ρ [Ω.m]. The seventeen resistivity values modelled are presented in the second line of Table 1. The relation between the electrical current density vector j [A/m²] and the potential E [V] is governed by Ohm's law:

$$j = -\frac{1}{\rho}\nabla E \qquad \text{Eq. 1}$$

In the system, the amount of current flux entering an enclosed surface of a material is equal to the amount of current leaving it (charge conservation):

$$\nabla . j = 0 \qquad \text{Eq. 2}$$

Two different boundary conditions are imposed on the concrete / rebar(s) interface(s) to model the two steps of the polarization. The polarization was divided in two distinct steps because the transcient evolution of the potential was not required to calculate the concrete cover resistivity and the rebar corrosion rate. The 3D geometry is complex and the model involves a large number of variables meaning that it would have been impossible to model the transcient polarization due to huge computer calculation duration. To model the instantaneous ohmic drop, a very small electric resistance (0.00001 Ω) is imposed because the capacitance of the Randles model (Figure 5 (a)) is short-circuited at that moment (Figure 5 (c)).

The Butler-Volmer equation (Eq. 1) is used to model the steady state response. Three of the four parameters of the Butler-Volmer equation are constant throughout this study and are presented in Table 2. The Tafel slopes cannot be measured on-site. Based on the chosen Tafel slopes, the coefficient B of the Stern-Geary equation is equal to 38 mV here which is between the usually assumed value of 26 mV for active state and 52 mV for passive state. The corrosion potential E_{corr} value has no impact on any of the results presented below; it only modifies the reference.

303 **Table 2. Butler-Volmer parameters used in this study.**

Parameter	Corrosion potential	Anodic Tafel slope	Cathodic Tafel slope
Symbol	E_{corr}	b_A	b_C
Value	- 0.42 V	0.3 V/dec	0.125 V/dec

304

305 The aim of this article is to determine the rebar corrosion rate, i_{corr}, with non-destructive tests
306 by using 3D numerical simulations to convert the data measured on the surface into the
307 corrosion rate. However, running the numerical model requires the corrosion rate, i_{corr}, to be
308 specified in the Butler-Volmer equation. This explains why an iterative approach is
309 developed. Three corrosion rates, 0.1, 0.5 and 1 $\mu A/cm^2$, are implemented in the Butler-
310 Volmer equation at the rebar / concrete interface. These three corrosion rate values
311 correspond to the upper transition value of negligible, low and moderate corrosion levels,
312 respectively [16]. A current density higher than 1 $\mu A/cm^2$ is considered as a high level of
313 corrosion. The iterative automatic treatment of the measured data will be presented in part 5.5
314 (Iterative measurement procedure).
315 All the other boundaries of the model are electrically isolated (no-flux boundary). The
316 simulations were performed for all the combinations of the parameters presented in Table 1,
317 corresponding to 25806 different cases. The different cases were modelled for the two steps
318 of the polarization.
319 Tetrahedral linear elements were used. Mesh refinement was performed on the probe and the
320 top parts of rebars. Several mesh refinement steps were applied until the potential was stable,
321 for all the modelled configurations.

5 Numerical results

The simulation is used to determine the surface linear polarization SLPR [Ω.m^2] which is the ratio between the rebar polarization and the current density at the PI:

$$R_{P,S} = \frac{\Delta E_P}{j_{PI}} \qquad \text{Eq. 4}$$

The corrosion rate calculation is different from that of the majority of other studies, where a polarization process is used. Most of the time, the LPR [Ω] is calculated as the ratio between the rebar polarization and the current. The assumed polarized area, A, is then used to determine the rebar corrosion rate (see Eq. 2). In this study, the corrosion rate is deduced from the SLPR without using an assumed polarization area:

$$i_{corr} = \frac{B}{R_{P,S}} \qquad \text{Eq. 5}$$

5.1 Example of a potential evolution

Figure 7 presents an example (D = 10 mm, c = 30 mm and ρ = 200 Ω.m) of the evolution of the potential along the vertical $\vec{z}$ axis (see Figure 6) obtained with Comsol Multiphysics. The dotted line represents the potential evolution at t = 0 (rebar is short-circuited) while the continuous line represents the steady state (Butler-Volmer equation for i_{corr} = 0.5 µA/cm^2). Once the galvanostatic current is applied, an instantaneous ohmic drop ΔE_Ω is observed on the surface. At this moment, the rebar is short-circuited, which explains why the potential on the rebar interface remains equal to the corrosion potential (E_{corr} = - 0.42 V in this example, see Table 2).

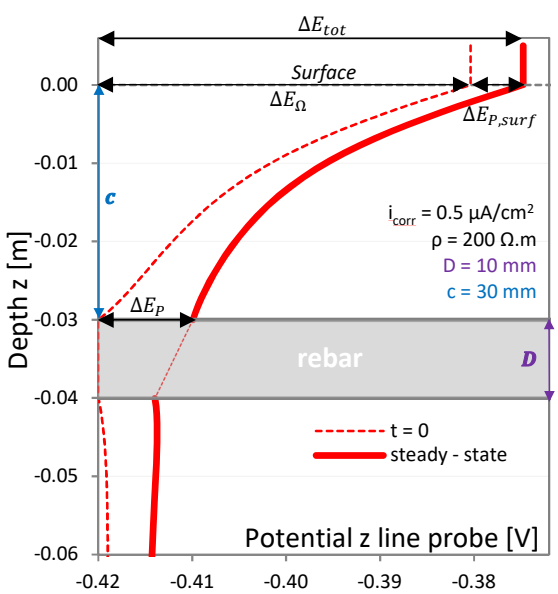

Figure 7. Potential evolution along the $\vec{z}$ axis at t = 0 (dotted line) and at steady state (continuous line) for i_{corr} = 0.5 µA/cm², D = 10 mm, c = 30 mm and ρ = 200 Ω.m.

At steady state, the rebar is polarized ($\Delta E_P \neq 0$). The difference between the potential measured on the surface ΔE_{tot} and the ohmic drop ΔE_Ω is called the polarization measured on the surface $\Delta E_{P,surf}$. Due to the three-dimensional nature of the problem, the polarization $\Delta E_{P,surf}$ is not equal to the rebar polarization ($\Delta E_P \neq \Delta E_{tot} - \Delta E_\Omega$). This explains the necessity for a 3D numerical simulation: the rebar polarization cannot be directly determined from the polarization measured on the surface as the relation between these two potentials depends on several parameters.

5.2 Influence of the supposed corrosion rate i_{corr}

The previous example was presented for a current density of 0.5 µA/cm². However, a different current and potential distribution is expected if the rebar corrosion rate, i_{corr} is modified. To illustrate this, Figure 8 is plotted for two additional corrosion rates, 0.1 and 1 µA/cm², while all the other parameters remain unchanged.

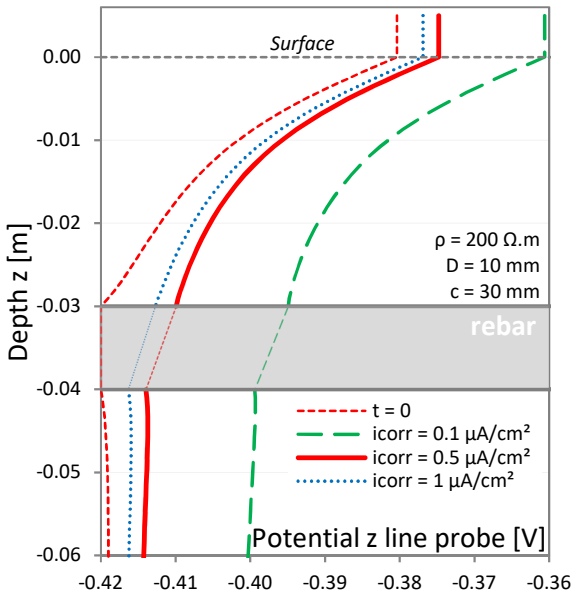

Figure 8. Potential evolution along the $\vec{z}$ axis at t = 0 (dotted line) and in steady state (continuous line) for i_{corr} = 0.5 µA/cm², (D = 10 mm, c = 30 mm and ρ = 200 Ω.m).

Figure 8 clearly shows that the potential measured on the surface, $\Delta E_{P,surf}$, and the rebar potential, ΔE_P, are significantly influenced by the rebar corrosion rate, i_{corr}. When the rebar corrosion rate decreases, the SLPR (and the LPR) increases, which explains the higher potential measured on the surface in the steady state. To determine the SLPR, both rebar polarization ΔE_P and j_{PI} are required.

In order to visualize the influence of the corrosion rate i_{corr} on both rebar polarization and current density at the PI, Figure 9 is plotted for a wide range of corrosion rates, i_{corr}, from 0.01 to 10 µA/cm² and for the same parameters as in Figure 7 and Figure 8 (D = 10 mm, c = 30 mm and ρ = 200 Ω.m).

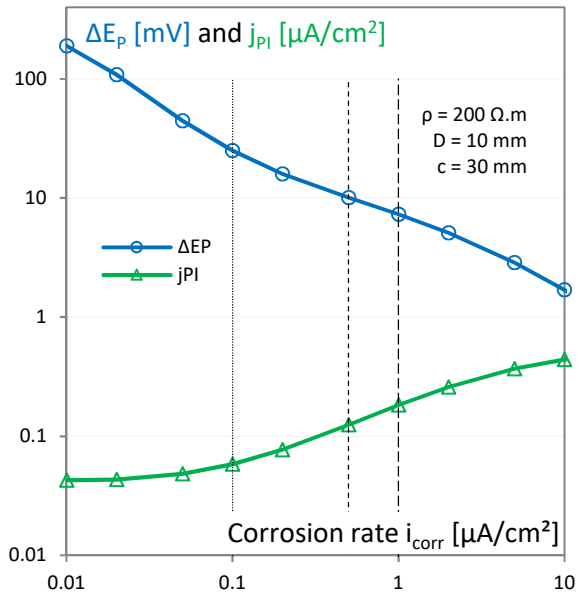

Figure 9. Rebar polarization ΔE_P (circles) and current density at the PI j_{PI} (triangles) depending on the corrosion rate, i_{corr}. (D = 10 mm, c = 30 mm and ρ = 200 Ω.m).

The three corrosion rates i_{corr} used for the numerical simulations (i.e. 0.1, 0.5 and 1 µA/cm²) are represented with dotted black vertical lines. As highlighted in Figure 8, the rebar polarization, ΔE_P, increases when the corrosion rate is numerically decreased. In contrast, the

current density at the PI increases with corrosion rate because SLPR reduction enables more current to flow through the interface right under the probe.

Thus, Figure 8 and Figure 9 enable us to understand that the current distribution is not only influenced by the concrete resistivity and geometrical parameters but also by the corrosion rate and this explains why this parameter was considered in an iterative measurement procedure that will be presented in detail in part 5.5. The influence of resistivity and the three geometrical parameters is first presented in parts 5.3 and 5.4.

5.3 Current density j_{PI}

To obtain the SLPR $R_{P,s}$ at the PI, both current density j_{PI} and rebar polarization ΔE_P are required. The current density at the PI should be influenced by the concrete resistivity, rebar spacing, cover and rebar diameter as it will modify the current line distribution. All these possible configurations were modelled numerically. This approach aimed first to determine j_{PI} on site, knowing the concrete cover resistivity ρ, rebar spacing s, concrete cover c and rebar diameter D. The ratio between j_{PI} and the current density injected by the CE j_P is shown in Figure 10 for a rebar diameter D of 10 mm. The current density injected by the CE j_P is constant ($j_P \approx 30\ \mu A/cm^2$) and is equal to the ratio between the injected current ($J_P = 10\ \mu A$) and the CE surface area.

A strong influence of the concrete resistivity on the current at the PI is revealed in Figure 10 (a) for a single bar. With high resistivity, a large part of the current flows directly from the CE to the PI. Lower resistivity enables wider current distribution over the concrete volume, explaining the lower proportion of current flowing through the PI which was also highlighted in [15,37].

Regardless of the concrete resistivity considered, the current density flowing through the PI decreases when the concrete cover is increased. As the concrete cover increases, the current is

spread farther along the rebar, explaining the lower current density right under the RE, at the PI.

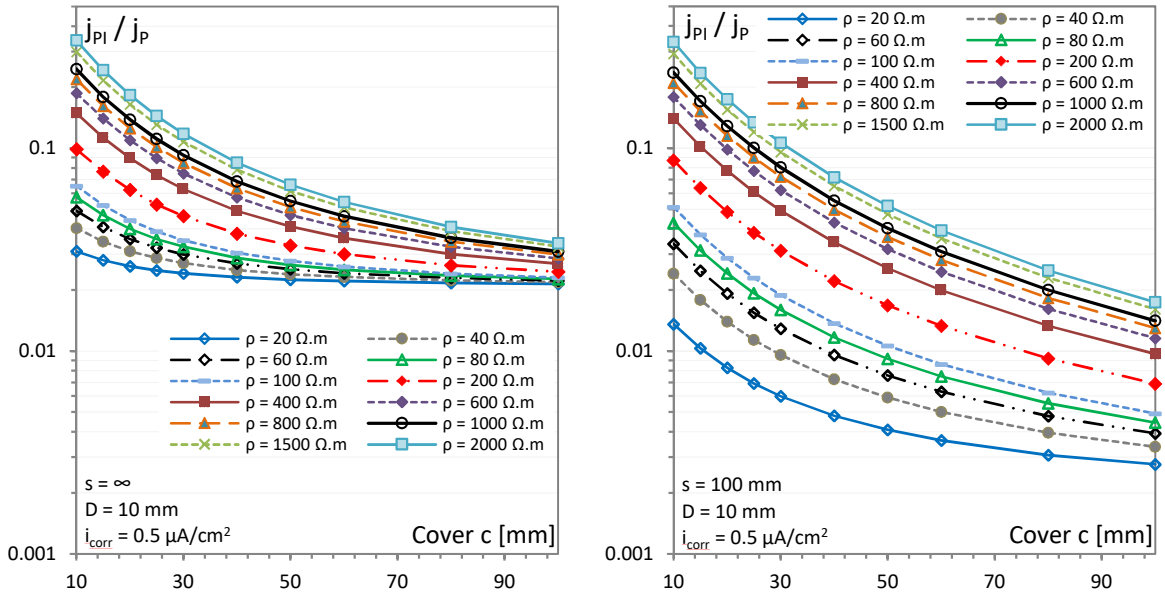

Figure 10. Ratio of the current density at the PI j_{PI} to the current density j_P injected by the CE for a 10 mm rebar diameter, depending on concrete cover for different concrete cover resistivities and for two rebar spacings, s = ∞ (a) and s = 100 mm (b).

Moreover, the current at the PI j_{PI} is also strongly influenced by the introduction of other rebars, as demonstrated in Figure 10 (b) for a rebar spacing, s, of 100 mm. For all the concrete covers and concrete resistivities, the introduction of other rebars is associated with a decrease of the current at the PI, j_{PI}. This is especially the case for the lower concrete resistivity because the current has other exit points that it can reach easily because of the low resistivity. The influence of both rebar diameter and rebar spacing on the ratio between j_{PI} and the current density injected by the CE, j_P, is quantified in Figure 11. In Figure 11 (a), only one rebar is considered (s = ∞). As previously observed, the current density at the PI decreases with concrete cover. The rebar diameter also influences the current distribution. With smaller diameter, the surface available for the current to pass is smaller, which explains why the

current density j_{PI} is higher. For a metal plate (D = ∞), the ratio j_{PI}/j_P is minimal because the current can flow out of the concrete through the larger available area.

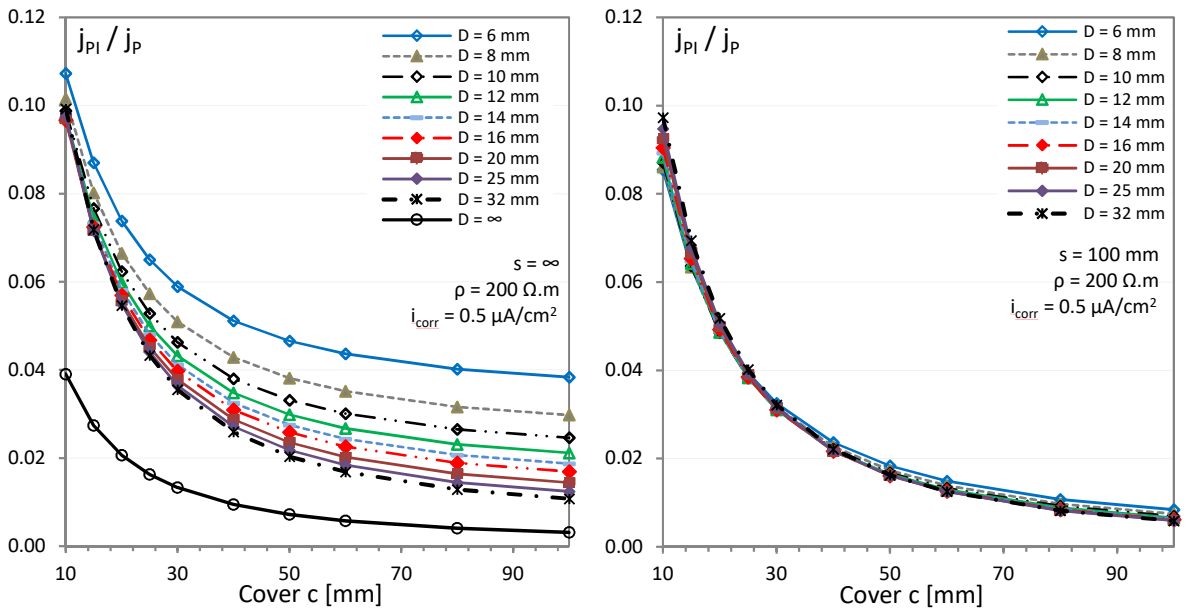

Figure 11. Ratio of the current density at the PI to injected current density j_P, for ρ = 200 Ω.m and for 2 rebar spacings: ∞ (a) and 100 mm (b).

Figure 11 (b) represents the same current density ratio when other rebars, spaced 100 mm apart, are introduced. Regardless of the rebar diameter or concrete cover considered, the current density at the PI is slightly decreased because of the presence of other rebars. These new rebars receive part of the injected current, which explains the current density reduction at the PI. However, because the resistivity is not very low, the introduction of other rebars does not modify the ratio j_{PI}/j_P very much for this particular example. It has already been demonstrated in Figure 10 (a) and (b) (ρ = 200 Ω.m - red dotted curve with diamond shaped markers) that the transition from a single bar to a 100 mm rebar spacing does not markedly modify j_{PI}/j_P for ρ = 200 Ω.m. Moreover, the differences observed in the ratio j_{PI}/j_P for the higher concrete covers (Figure 11 (a)) are now negligible. These two figures give an understanding of the influence of rebar diameter and rebar spacing on the current density at the PI j_{PI}. This demonstration concerns a concrete resistivity of 200 Ω.m and a corrosion rate

of 0.5 µA/cm^2 but similar conclusions can be obtained for other concrete resistivities and corrosion rates.

5.4 Rebar polarization ΔE_P

To determine the SLPR, the rebar polarization ΔE_P is also required. The concrete cover and resistivity, and the rebar diameter and spacing influence the current distribution and, again, have to be taken into account to determine the rebar polarization.

The example in Figure 7 demonstrates that the rebar polarization and the polarization measured on the surface are not equal (see also schematic layout in Figure 5 (d)). In order to determine the rebar polarization, ΔE_P, based on the potential measured on the surface $\Delta E_{P,surf}$, Figure 12 shows an example of 10 mm rebar(s). For a single bar (Figure 12 (a)) and resistivity lower than or equal to 100 Ω.m, the ratio $\Delta E_P/\Delta E_{P,surf}$ decreases when the concrete cover increases. Different behaviour is observed for resistivity higher than 100 Ω.m: the ratio is maximal for concrete covers of around 20 mm, which is usually the case on site.

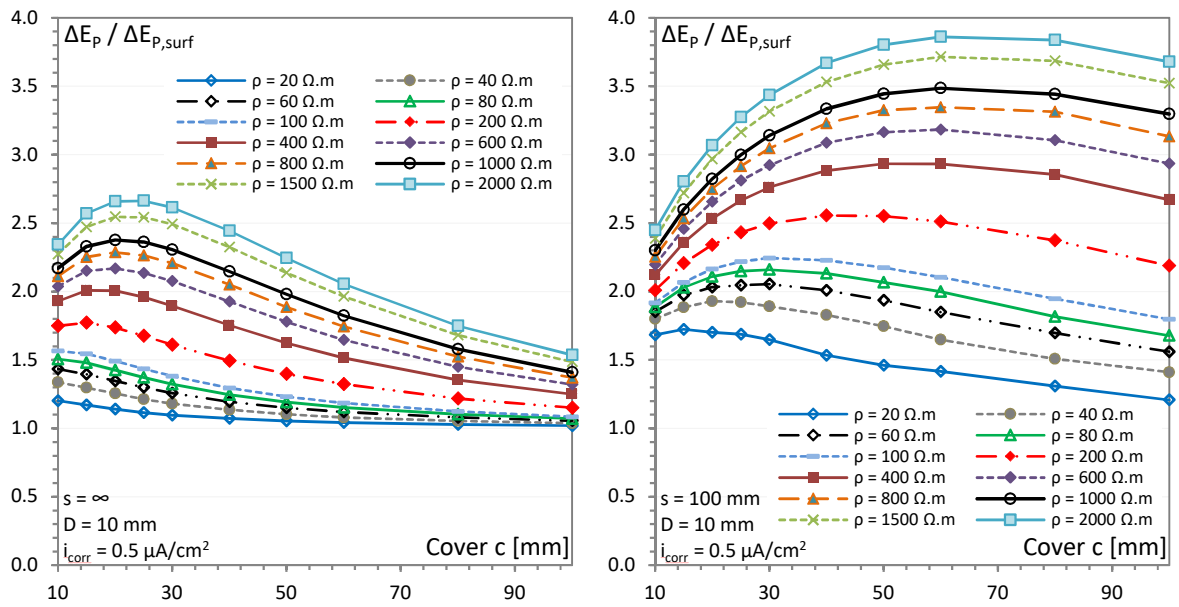

Figure 12. Ratio of the rebar polarization to the polarization measured on the surface for a 10 mm diameter rebar, according to concrete cover depth for different concrete cover resistivities and for two rebar spacings, s = ∞ (a) and s = 100 mm (b).

It can be observed on Figure 12 that the rebar polarization, ΔE_P, is always higher than the polarization measured on the surface, $\Delta E_{P,surf}$. Thus, if the rebar polarization is wrongly determined as the difference between the polarization measured on the surface in the steady state minus the instantaneous ohmic drop, the rebar polarization and the SLPR are overestimated. Thus, the corrosion rate can be dangerously underestimated.

The fact that the $\Delta E_P/\Delta E_{P,surf}$ ratio increases with resistivity can be explained by the fact that higher resistivity leads to more concentrated current lines right under the CE. As observed for the ratio j_{PI}/j_P, the ratio $\Delta E_P/\Delta E_{P,surf}$ is also influenced by the introduction of other rebars as demonstrated in Figure 12 (b). The ratio $\Delta E_P/\Delta E_{P,surf}$ increases significantly with the introduction of other rebars because their presence tends to decrease the resistance of the system, leading to a decrease of the polarization measured at the surface.

The influence of rebar diameter is presented in Figure 13 for a 200 Ω.m resistivity and two rebar spacings (s = ∞ (a) and s = 100 mm (b)). As demonstrated for the ratio j_{PI}/j_P (Figure 11), the ratio $\Delta E_P/\Delta E_{P,surf}$ is also influenced by the rebar diameter, whatever the spacing factor considered.

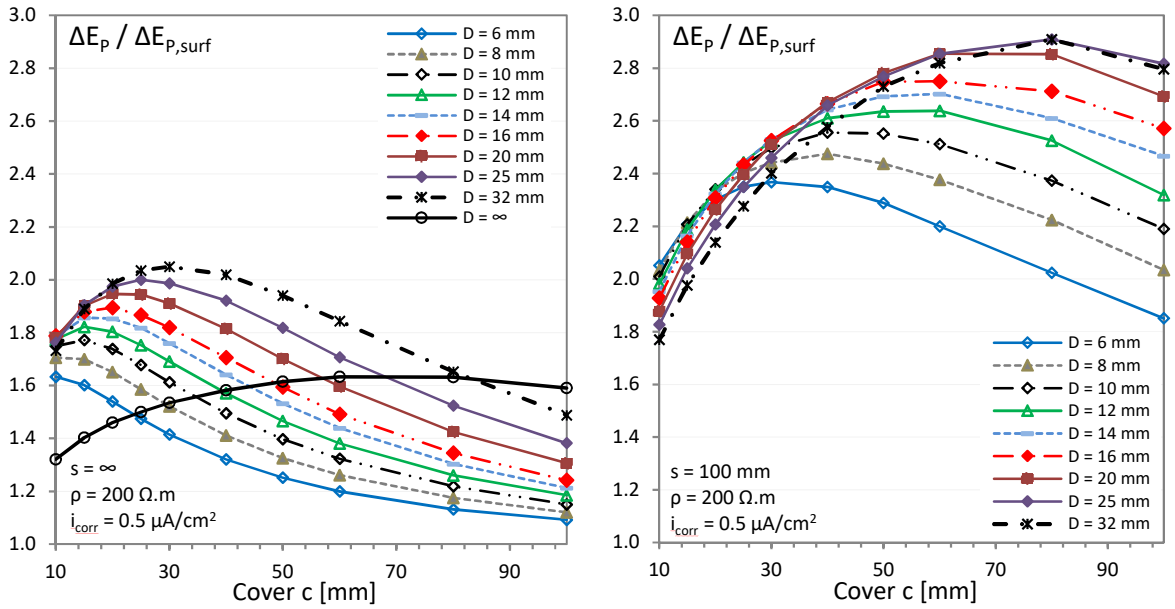

Figure 13. Ratio of the rebar polarization to the polarization measured on the surface according to concrete cover for various rebar and for two rebar spacings, s = ∞ (a) and s = 100 mm (b).

For a metal plate (D = ∞), the ratio $\Delta E_P/\Delta E_{P,surf}$ exhibits a different evolution according to the concrete cover, which is associated with a different current distribution in the concrete. The previous graphs (Figure 10, Figure 11, Figure 12, Figure 13) were obtained for a numerical corrosion rate of 0.5 µA/cm^2. As significantly different values of these ratios were obtained with the two other corrosion rates modelled (i.e. i_{corr} of 0.1 and 1 µA/cm^2), an iterative approach was developed and is presented in the next part.

5.5 Iterative measurement procedure

In order to visualize the influence of the supposed corrosion rate in the calculation of corrosion rate, Figure 14 is introduced. It presents the error of the calculated corrosion current density $i_{corr,calculated}$ depending on the corrosion current density i_{corr} for an example with a single 10 mm diameter rebar, a concrete cover of 30 mm and a concrete cover resistivity of 200 Ω.m. This error was represented for three supposed corrosion current density (i.e. 0.1, 0.5 and 1 µA/cm^2). The calculated corrosion rates $i_{corr,calculated}$ were calculated using the potential measured on the surface, $\Delta E_{P,surf}$ and the ratios j_{PI}/j_P and $\Delta E_P/\Delta E_{P,surf}$ determined for each supposed corrosion rate. It is clear in Figure 14 that the calculated corrosion rate $i_{corr,calculated}$ is equal to the corrosion current density i_{corr} when the supposed corrosion rate is correct (error = 0 % in Figure 14). Figure 14 also revealed that it is very important to use a supposed corrosion rate close to the real corrosion rate. For instance, if the rebar corrosion rate is 0.1 µA/cm² (purple dotted vertical curve) and the supposed corrosion rate is 1 µA/cm² (red curve

with square markers), the error reach 76 %. The error measured can be important which explain that an iterative approach must be performed.

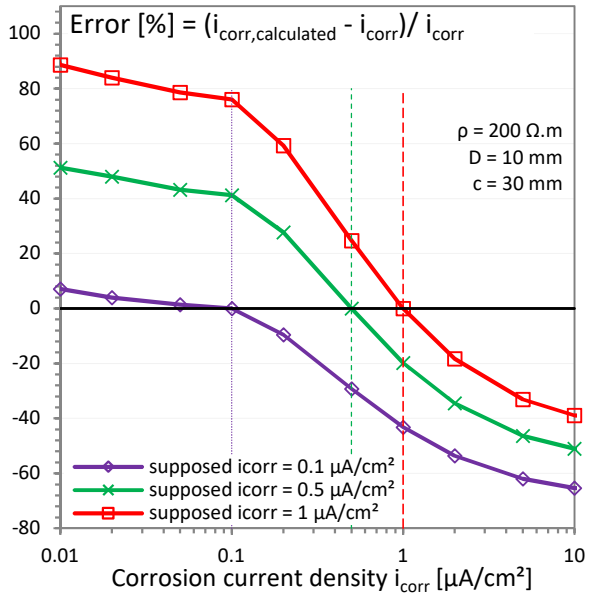

Figure 14. Error in corrosion rate calculation depending on the corrosion rate of the rebar for three supposed corrosion rate (0.1, 0.5 and 1 µA/cm²). This example is presented for a single bar, D = 10 mm, c = 30 mm and ρ = 200 Ω.m.

The on-site measurement process and the automatic iterative corrosion rate calculation is detailed in Figure 15. The different potentials (E_{corr}, ΔE_{tot} and ΔE_{Ω}) useful for SLPR measurement are recorded by the RE during the transient polarization measurement and are employed for SLPR measurement here thanks the graphs plotted for j_{PI}/j_P and $\Delta E_P/\Delta E_{P,surf}$. The left part of Figure 15 deals with the resistivity calculation and is similar to what was presented in a previous article [8].

The right part presents the algorithm used for rebar corrosion rate estimation. The three supposed values of corrosion rate employed for numerical simulations (0.1, 0.5 and 1 µA/cm^2) are stored in the vector $i_{corr,vec}$. The ratios j_{PI}/j_P and $\Delta E_P/\Delta E_{P,surf}$ are determined

using the simulations based on the first value of $i_{corr,vec,1}$ (i.e. 0.1 μA/cm^2 here) depending on the resistivity calculated in the left part of Figure 15.

The ratios j_{PI}/j_P and $\Delta E_P/\Delta E_{P,surf}$ are calculated for a limited number of modelled resistivities (17 different resistivities, see Table 1). The resistivities measured on site are different from the resistivities modelled. Some linear interpolations between the graphs obtained with the adjacent modelled resistivity and the resistivity measured on site are automatically calculated by the software developed by the authors to obtain a more accurate estimation of the j_{PI}/j_P and $\Delta E_P/\Delta E_{P,surf}$ ratios.

Using these two ratios for the first supposed corrosion rate $i_{corr,vec,1}$ and the measured potential $\Delta E_{P,surf}$, SLPR and then the first corrosion rate, $i_{corr,1}$, can be calculated and compared to the supposed corrosion rate $i_{corr,vec,1}$. If the calculated value is lower than $i_{corr,vec,1}$, which is the smallest corrosion rate for which the simulations were performed, the calculated value is kept and corresponds to a negligible corrosion rate. If the calculated value is higher, a second corrosion rate is calculated using the second supposed corrosion rate (i.e. $i_{corr,vec,2}$ = 0.5 μA/cm^2 here). If the second calculated corrosion rate value $i_{corr,2}$ is higher than the second supposed corrosion rate value $i_{corr,vec,2}$, another iterative loop is performed. Otherwise, if $i_{corr,2} < i_{corr,vec,2}$ (i.e. $0.1 < i_{corr,2} < 0.5$ μA/cm^2 here), the final output corrosion rate value i_{corr} is determined using a weighted average between the first and the second calculated values ($i_{corr,1}$ and $i_{corr,2}$). The highest weight is given to the calculated value that is closest to the supposed value. Finally, after all the possible iterative looping (i.e. a maximum of three loops here), if the last calculated value is higher than the supposed value, the final output corrosion rate value i_{corr} will be the last one calculated.

This algorithm may appear unnecessarily complex as the simulations have only been performed for three corrosion rates, i_{corr}, for the moment. However, additional supposed

corrosion rates will be progressively added in order to increase the precision of the calculation and this is why the algorithm is presented in its most general form.

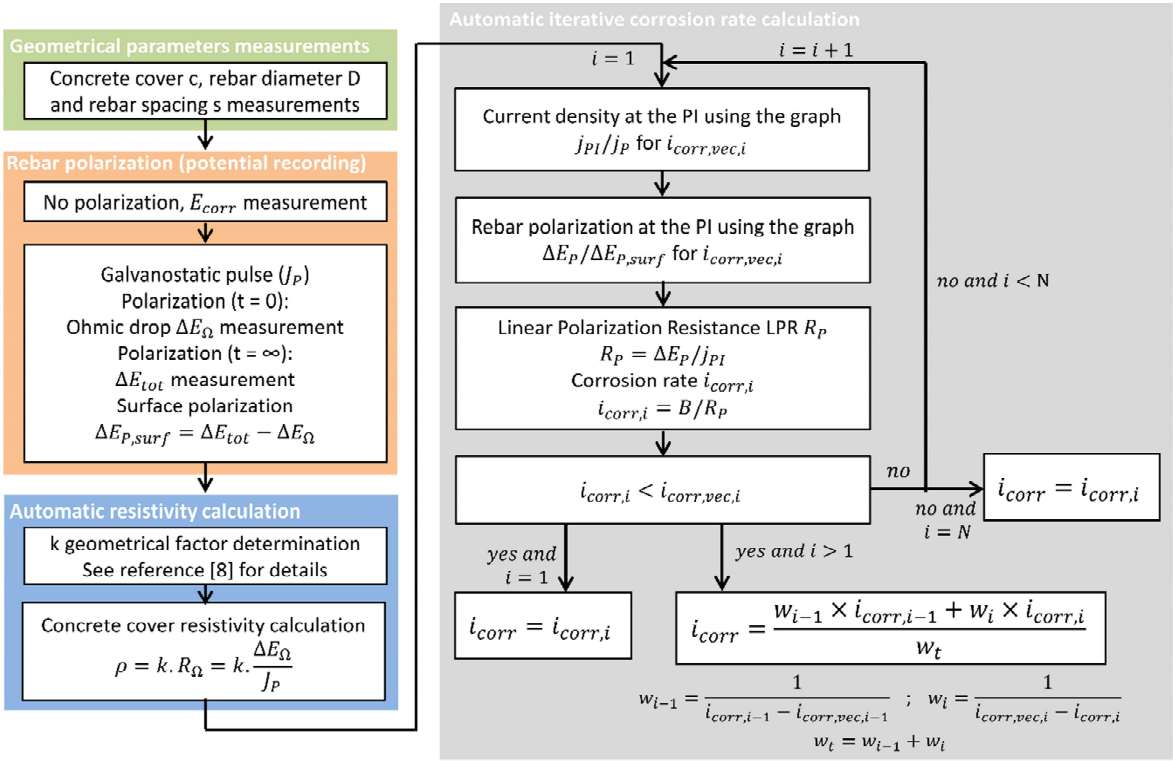

Figure 15. Procedure for the SLPR and corrosion rate measurement on site.

6 Experimental measurements

The probe and associated measurement procedure were used to determine the rebar corrosion potential, concrete cover resistivity and rebar corrosion rate on the rebars of eight slabs during 18 weeks. In order to limit the number of figures in this article, we chose to calculate the average value of these parameters for the six concrete covers (Figure 3) at each time point and to present the results in three figures (Figure 16, Figure 17, Figure 18).

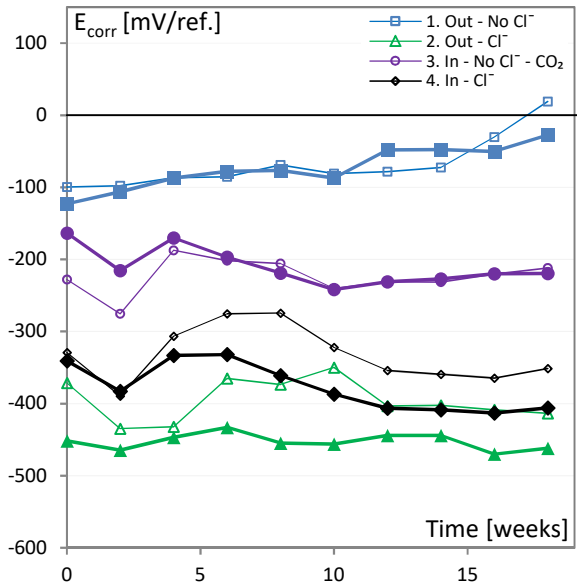

Figure 16. Evolution of the average corrosion potential E_{corr} measured on the eight slabs. Thick curves are for 20 mm rebars, thin curves are for 6 mm rebars.

The evolution of the corrosion potentials is presented in Figure 16. The first notable feature is that, whatever the curing condition considered, the two rebars in the same curing conditions follow the same general trend. However, for both concrete slabs containing chloride (cures 2 and 4) the corrosion potential is lower (around 50 mV/ref) for 20 mm rebars.

The slabs without chloride, placed outdoors (cure 1) present the highest corrosion potential. During the 18 weeks of measurements, the corrosion potential increased slightly, from around - 100 mV/ref. to 0 mV/ref., which indicates an extremely low corrosion risk. In contrast, the slabs containing chlorides and placed outdoors have the lowest corrosion potentials observed. They are around – 430 mV/ref. after 18 weeks, which indicates high corrosion risk. The slabs prepared without chloride and placed in an ordinary indoor environment (cure 4) or placed in the carbonation chamber (cure 3) have intermediate corrosion potentials. The corrosion potentials of slabs prepared with chlorides and placed indoors are around - 200 mV/ref., which indicates that the carbonation front probably reached the rebars. The extremely high water/cement ratio led to very high porosity and the CO_2 content of the carbonation chamber

(50 %) was very high. These two facts explain the fast carbonation and associated intermediate corrosion potentials observed. Finally, the slabs stored indoors and prepared with chloride exhibit low corrosion potentials (around - 370 mV/ref.). As observed for the other slabs prepared with chloride and stored outside (cure 2), the high chloride content introduced during slab fabrication probably avoided the formation of a passive layer.

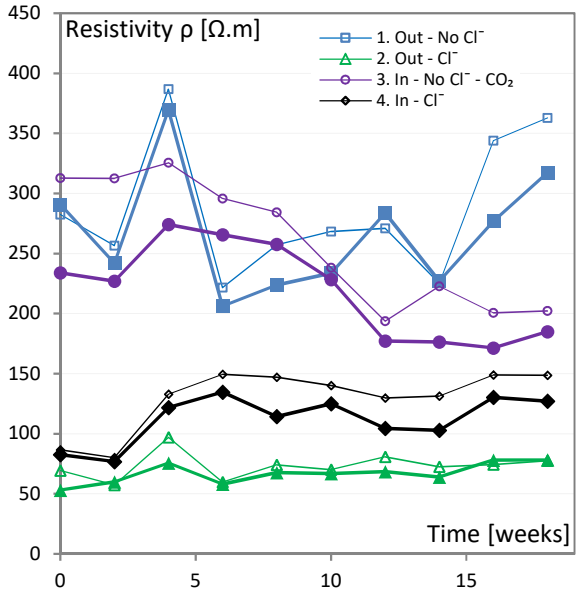

Figure 17. Evolution of the average concrete cover resistivity ρ measured on the eight slabs. Thick curves are for 20 mm rebars, thin curves are for 6 mm rebars.

The concrete cover resistivity evolution is presented in Figure 17. On the one hand, the slabs prepared without chloride and placed outdoors exhibit the highest concrete cover resistivity variation, which can be attributed to the hydrothermal variations (rain, temperature, etc.). Resistivities are between 200 and 400 Ω.m, which is quite small for concrete but can be explained by the extremely high water/binder ratio. The average coefficient of variation (standard deviation / average) is 19% for these two slabs (cure 1).

On the other hand, the slabs kept in the same conditions but prepared with chloride (cure 2) have very low resistivity (around 70 Ω.m). The presence of chloride logically decreased the concrete resistivity of the specimens and the average coefficient of variation is 14%.. Again,

the slabs placed indoors, prepared with chloride (cure 4) and placed in the carbonation chamber (cure 3) present intermediate behaviours. The resistivity of the slabs stored indoors and prepared with chloride have low values that seem to be nearly stable (average of 120 Ω.m, average coefficient of variation of 19%) at the end of the 18 weeks of experiments. The slabs placed indoors under carbonation (50% CO_2 and 65% RH - cure 3) show slightly decreasing resistivity values that seem to have stabilized around 180 Ω.m.

The measured resistivities are in agreement with the two different exposure conditions and the presence or absence of chloride. Note that the measured values are relatively low compared to what can be measured on site for ordinary concrete because of the low performance concrete employed.

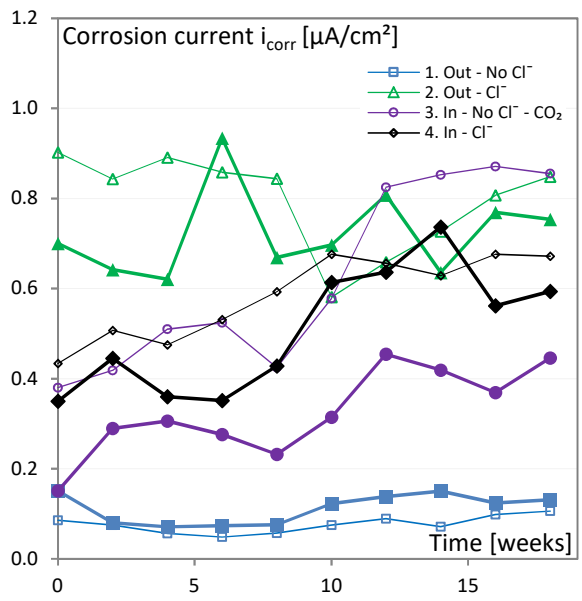

Figure 18. Evolution of the average corrosion rate i_{corr} measured on the eight slabs. Thick curves are for 20 mm rebars, thin curves are for 6 mm rebars. Curves numbered 2 and 4 are false because they were calculated assuming uniform corrosion.

Finally, corrosion rate evolution is presented in Figure 18. The lowest corrosion rate values were obtained for the slabs placed outdoors and prepared without chloride. The measured

values are not negligible as some of them are higher than 0.1 µA/cm² (see corrosion levels in [16]).

The corrosion rate of the slab placed in the carbonation chamber is already high, which indicates that the rebar passivated layer was destroyed due to the fast ingress of CO_2. This is in agreement with the measured corrosion potentials (Figure 16).

The measurement procedure developed in this paper is based on uniform corrosion. However, different papers [43–45] have proved that the chloride ingress causes macrocell corrosion in which the active anode and the passive cathode are spatially separated. It is currently impossible to determine the active surface area, and thus to calculate the local corrosion rate, without destructive tests. The corrosion values obtained on both slabs containing chloride (cures 2 and 4) are presented but the authors insist on the fact that the corrosion rate values presented are not correct. They are apparent corrosion rates. At the end of the 18 weeks of experiments, based on the method developed, which assumes uniform corrosion, the estimated corrosion rates measured on these two slabs were between 0.6 and 1.2 µA/cm^2. These values are certainly underestimated as the local corrosion rate at the anode might be much higher. Thus, this probe and the associated measurement principle cannot be applied to determine the corrosion rate when concrete is in presence of chlorides but an apparent corrosion rate can be calculated. As far as we know, there are no devices that can be employed at present to non-destructively determine the rebar corrosion rate for macrocell corrosion. However, the evolution of the apparent corrosion rate will give precious information concerning the evolution of the corrosion state of the structure under inspection. Moreover, the probe and associated measurement principle can be used to determine both the rebar corrosion potential (no polarization) and the concrete cover resistivity as the rebar is short-circuited in both micro and macrocell corrosion

7 Conclusions

A new probe with a smaller counter electrode than in previous probes has been developed in order to evaluate the corrosion state of reinforced concrete structures. An electrical connection has to be made to the rebar and then galvanostic polarization is performed. No guard ring is used. Three-dimensional numerical simulations are the only way to reliably understand the distribution of polarizing current. In that way, the measurement was numerically modelled in order to convert the potential evolution measured on the surface to the rebar corrosion rate. The following conclusions can be drawn:

- It is necessary to take the three geometrical parameters of the problem (rebar spacing, s, concrete cover, c, and rebar diameter, D) and the concrete resistivity into account for SLPR $R_{P,s}$ evaluation as they modify the current and potential distribution through the concrete.
- The polarization measured on the surface, $\Delta E_{P,surf}$, is smaller than the rebar polarization, ΔE_P. The $\Delta E_P/\Delta E_{P,surf}$ ratio is determined numerically and graphs are also proposed in order to convert the potential surface measurement easily.
- The current density at the Point of Interest, j_{PI}, decreases when the rebar spacing decreases, when the concrete cover increases, or when the rebar diameter increases. Decreasing the concrete resistivity and the rebar corrosion rate also decreases the current density at the PI. The j_{PI}/j_P ratio is determined numerically in order evaluate the current density at the PI easily.

A complete methodology for the exploitation of the measurement is finally proposed based on charts and an iterative procedure.

The three corrosion parameters evaluated (corrosion potential, concrete cover and rebar corrosion rate) were in good agreement with the composition of the slabs and their curing conditions. However, to improve the iterative measurement procedure developed in this study,

other numerical simulations need to be performed with other assumed corrosion rates. The numerical model is also based on a uniform concrete resistivity. However, on site, a resistivity gradient is usually observed and it will modify the measurement. The resistivity measurement method must be validated using other device such as the Wenner on samples without rebars. Moreover, the validation should be performed on concrete that present higher resistivity which would be more representative to field environment. Finally, in order to evaluate the precision of the methodology developed here for corrosion rate assessement, a comparative study between non-destructive measurements made with the DIAMOND probe and destructive mass loss measurements will be carried out.

8 References

[1] L. Bertolini, B. Elsener, P. Pedeferri, E. Redaelli, R. Polder, Corrosion of Steel in Concrete: Prevention, Diagnosis, Repair, 2nd Edition, Wiley.Com. (2017).

[2] P. Ghods, O.B. Isgor, M. Pour-Ghaz, A practical method for calculating the corrosion rate of uniformly depassivated reinforcing bars in concrete, Mater. Corros. 58 (2007) 265–272. https://doi.org/10.1002/maco.200604010.

[3] K. Reichling, M. Raupach, J. Broomfield, J. Gulikers, P.V. Nygaard, U. Schneck, G. Sergi, Local detailed inspection methods regarding reinforcement corrosion of concrete structures, Mater. Corros. 64 (2013) 128–134. https://doi.org/10.1002/maco.201206626.

[4] B. Yu, J. Liu, Z. Chen, Probabilistic evaluation method for corrosion risk of steel reinforcement based on concrete resistivity, Constr. Build. Mater. 138 (2017) 101–113. https://doi.org/10.1016/j.conbuildmat.2017.01.100.

[5] W.J. McCarter, H.M. Taha, B. Suryanto, G. Starrs, Two-point concrete resistivity measurements: interfacial phenomena at the electrode–concrete contact zone, Meas. Sci. Technol. 26 (2015) 085007. https://doi.org/10.1088/0957-0233/26/8/085007.

[6] M.G. Alexander, Y. Ballim, K. Stanish, A framework for use of durability indexes in performance-based design and specifications for reinforced concrete structures, Mater. Struct. 41 (2008) 921–936. https://doi.org/10.1617/s11527-007-9295-0.

[7] K. Reichling, M. Raupach, N. Klitzsch, Determination of the distribution of electrical resistivity in reinforced concrete structures using electrical resistivity tomography: ERT on reinforced concrete, Mater. Corros. 66 (2015) 763–771. https://doi.org/10.1002/maco.201407763.

[8] G. Samson, F. Deby, J.-L. Garciaz, J.-L. Perrin, A new methodology for concrete resistivity assessment using the instantaneous polarization response of its metal reinforcement framework, Constr. Build. Mater. 187 (2018) 531–544. https://doi.org/10.1016/j.conbuildmat.2018.07.158.

[9] C. Alonso, C. Andrade, J.A. González, Relation between resistivity and corrosion rate of reinforcements in carbonated mortar made with several cement types, Cem. Concr. Res. 18 (1988) 687–698. https://doi.org/10.1016/0008-8846(88)90091-9.
[10] G.K. Glass, C.L. Page, N.R. Short, Factors affecting the corrosion rate of steel in carbonated mortars, Corros. Sci. 32 (1991) 1283–1294. https://doi.org/10.1016/0010-938X(91)90048-T.
[11] K. Hornbostel, C.K. Larsen, M.R. Geiker, Relationship between concrete resistivity and corrosion rate – A literature review, Cem. Concr. Compos. 39 (2013) 60–72. https://doi.org/10.1016/j.cemconcomp.2013.03.019.
[12] P.V. Nygaard, M.R. Geiker, Measuring the corrosion rate of steel in concrete – effect of measurement technique, polarisation time and current, Mater. Corros. 63 (2012) 200–214. https://doi.org/10.1002/maco.201005792.
[13] B. Yu, L. Yang, M. Wu, B. Li, Practical model for predicting corrosion rate of steel reinforcement in concrete structures, Constr. Build. Mater. 54 (2014) 385–401. https://doi.org/10.1016/j.conbuildmat.2013.12.046.
[14] C. Andrade, C. Alonso, J. Sarría, Corrosion rate evolution in concrete structures exposed to the atmosphere, Cem. Concr. Compos. 24 (2002) 55–64. https://doi.org/10.1016/S0958-9465(01)00026-9.
[15] A. Fahim, P. Ghods, O.B. Isgor, M.D.A. Thomas, A critical examination of corrosion rate measurement techniques applied to reinforcing steel in concrete, Mater. Corros. 69 (2018) 1784–1799. https://doi.org/10.1002/maco.201810263.
[16] C. Andrade, C. Alonso, Test methods for on-site corrosion rate measurement of steel reinforcement in concrete by means of the polarization resistance method, Mater. Struct. 37 (2004) 623–643. https://doi.org/10.1007/BF02483292.
[17] M.B. Otieno, H.D. Beushausen, M.G. Alexander, Corrosion propagation in reinforced concrete structures - state of the art review and way forward, in: CONSEC'10 - Mexico, 2010: pp. 461–469.
[18] A.M. Neville, Properties of Concrete, Édition : 5, Prentice Hall, Harlow, England; New York, 2011.
[19] S.G. Millard, D. Law, J.H. Bungey, J. Cairns, Environmental influences on linear polarisation corrosion rate measurement in reinforced concrete, NDT E Int. 34 (2001) 409–417. https://doi.org/10.1016/S0963-8695(01)00008-1.
[20] H.S. So, S.G. Millard, On-Site Measurements on Corrosion Rate of Steel in Reinforced Concrete, ACI Mater. J. 104 (2007).
[21] A. Michel, P.V. Nygaard, M.R. Geiker, Experimental investigation on the short-term impact of temperature and moisture on reinforcement corrosion, Corros. Sci. 72 (2013) 26–34. https://doi.org/10.1016/j.corsci.2013.02.006.
[22] S. Laurens, P. Hénocq, N. Rouleau, F. Deby, E. Samson, J. Marchand, B. Bissonnette, Steady-state polarization response of chloride-induced macrocell corrosion systems in steel reinforced concrete — numerical and experimental investigations, Cem. Concr. Res. 79 (2016) 272–290. https://doi.org/10.1016/j.cemconres.2015.09.021.
[23] M. Stern, A.L. Geary, Electrochemical Polarization I . A Theoretical Analysis of the Shape of Polarization Curves, J. Electrochem. Soc. 104 (1957) 56–63. https://doi.org/10.1149/1.2428496.
[24] J. Ge, O.B. Isgor, Effects of Tafel slope, exchange current density and electrode potential on the corrosion of steel in concrete, Mater. Corros. 58 (2007) 573–582. https://doi.org/10.1002/maco.200604043.
[25] Z.-T. Chang, B. Cherry, M. Marosszeky, Polarisation behaviour of steel bar samples in concrete in seawater. Part 1: Experimental measurement of polarisation curves of steel in concrete - ScienceDirect, Corros. Sci. 50 (2008) 357–364.

[26] G. Song, Theoretical analysis of the measurement of polarisation resistance in reinforced concrete, Cem. Concr. Compos. 22 (2000) 407–415. https://doi.org/10.1016/S0958-9465(00)00040-8.
[27] I. Martínez, C. Andrade, Polarization resistance measurements of bars embedded in concrete with different chloride concentrations: EIS and DC comparison, Mater. Corros. 62 (2011) 932–942. https://doi.org/10.1002/maco.200905596.
[28] J.A. González, A. Molina, M.L. Escudero, C. Andrade, Errors in the electrochemical evaluation of very small corrosion rates—I. Polarization resistance method applied to corrosion of steel in concrete, Corros. Sci. 25 (1985) 917–930. https://doi.org/10.1016/0010-938X(85)90021-6.
[29] G.K. Glass, An assessment of the coulostatic method applied to the corrosion of steel in concrete, Corros. Sci. 37 (1995) 597–605. https://doi.org/10.1016/0010-938X(94)00156-Z.
[30] M.E. Mitzithra, Detection of corrosion of reinforced concrete on cooling towers of energy production sites, PhD Thesis, University of Toulouse III - Paul Sabatier, 2013. http://thesesups.ups-tlse.fr/2135/ (accessed August 29, 2016).
[31] M.E. Mitzithra, F. Deby, J.P. Balayssac, J. Salin, Proposal for an alternative operative method for determination of polarisation resistance for the quantitative evaluation of corrosion of reinforcing steel in concrete cooling towers, Nucl. Eng. Des. 288 (2015) 42–55. https://doi.org/10.1016/j.nucengdes.2015.03.018.
[32] A. Clément, S. Laurens, G. Arliguie, F. Deby, Numerical study of the linear polarisation resistance technique applied to reinforced concrete for corrosion assessment, Eur. J. Environ. Civ. Eng. 16 (2012) 491–504. https://doi.org/10.1080/19648189.2012.668012.
[33] S. Laurens, A. Clément, G. Arliguie, F. Deby, APPLET - Simulation numérique de la mesure de resistance de polarisation lineaires des armatures du beton, 2010.
[34] P.V. Nygaard, M.R. Geiker, B. Elsener, Corrosion rate of steel in concrete: evaluation of confinement techniques for on-site corrosion rate measurements, Mater. Struct. 42 (2009) 1059–1076. https://doi.org/10.1617/s11527-008-9443-1.
[35] O.K. Gepraegs, C.M. Hansson, A Comparative Evaluation of Three Commercial Instruments for Field Measurements of Reinforcing Steel Corrosion Rates, J. ASTM Int. 2 (2005) 1–16. https://doi.org/10.1520/JAI11789.
[36] M. Raupach, B. Elsener, R. Polder, J. Mietz, Corrosion of Reinforcement in Concrete: Monitoring, Prevention and Rehabilitation Techniques, Woodhead Publishing, 2014.
[37] P.V. Nygaard, Non-destructive elecrochemical monitoring of reinforcement corrosion, Technical University of Denmark (DTU), 2009.
[38] S. Feliu, J.A. González, J.M. Miranda, V. Feliu, Possibilities and problems of in situ techniques for measuring steel corrosion rates in large reinforced concrete structures, Corros. Sci. 47 (2005) 217–238. https://doi.org/10.1016/j.corsci.2004.04.011.
[39] J.A. González, J.M. Miranda, S. Feliu, Considerations on reproducibility of potential and corrosion rate measurements in reinforced concrete, Corros. Sci. 46 (2004) 2467–2485. https://doi.org/10.1016/j.corsci.2004.02.003.
[40] DIAMOND project, Proj. Diam. - Diagn. Corros. Béton Armé - Sonde Captae. (2017). https://www.projet-diamond.com.
[41] B. Elsener, Corrosion rate of steel in concrete - Measurements beyond the Tafel law, Corros. Sci. 47 (2005) 3019–3033. https://doi.org/10.1016/j.corsci.2005.06.021.
[42] G. Klysz, J.-P. Balayssac, S. Laurens, Spectral analysis of radar surface waves for non-destructive evaluation of cover concrete, NDT E Int. 37 (2004) 221–227. https://doi.org/10.1016/j.ndteint.2003.09.006.
[43] U. Angst, Challenges and opportunities in corrosion of steel in concrete | SpringerLink, Mater. Struct. 51 (2018) 1–20. https://doi.org/10.1617/s11527-017-1131-6.

[44] C. Chalhoub, R. François, M. Carcasses, Determination of chloride threshold initiating corrosion: A new set-up taking the localized aspect of corrosion into account, Cem. Concr. Res. 124 (2019) 105825. https://doi.org/10.1016/j.cemconres.2019.105825.

[45] C. Chalhoub, R. François, D. Garcia, S. Laurens, M. Carcasses, Macrocell corrosion of steel in concrete: Characterization of anodic behavior in relation to the chloride content, Mater. Corros. n/a (2020). https://doi.org/10.1002/maco.201911398.